ACS Photonics

pubs.acs.org/journal/apchd5

Article

Nanocrystal-Based Active Photonics Device through Spatial Design of Light-Matter Coupling

Tung Huu Dang, Adrien Khalili, Claire Abadie, Charlie Gréboval, Mariarosa Cavallo, Huichen Zhang, Erwan Bossavit, James K. Utterback, Erwan Dandeu, Yoann Prado, Gregory Vincent, Sandrine Ithurria, Yanko Todorov, Carlo Sirtori, Angela Vasanelli,* and Emmanuel Lhuillier*

Cite This: https://doi.org/10.1021/acsphotonics.2c00738

Read Online

ACCESS | Metrics & More | Article Recommendations | Supporting Information

ABSTRACT: The integration of photonic structures in nanocrystal (NC)-based photodetectors has been demonstrated to improve device performances. Furthermore, bias-dependent photoresponse can be observed in such devices as a result of the interplay between hopping transport and inhomogeneous electromagnetic field. Here, we investigate the main physical concepts leading to a voltage-dependent photoresponse. We first bring evidence of bias-dependent carrier mobilities in a NC array over a wide range of temperatures. Then, we fabricate an infrared sensing device using HgTe NCs, where the electrodes also play the role of a grating, inducing a spatially inhomogeneous absorption. The obtained device exhibits a significant bias-dependent photoresponse while possessing a competitive detection performance in the extended short-wave and mid-wave infrared, with detectivity reaching 7×10^{10} Jones at 80 K and a fast response time of around 70 ns. This work provides the foundation for further advancements in NC-based-active photonics devices.

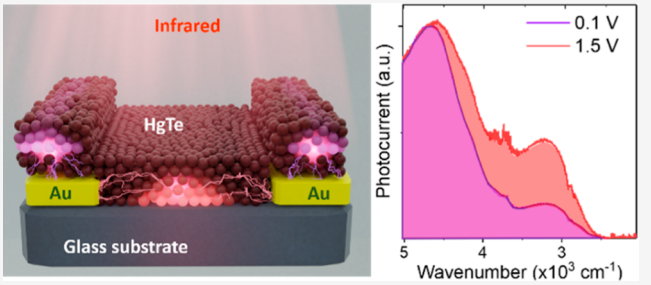

KEYWORDS: *nanocrystals, carrier mobility, infrared, active photonics, light matter coupling*

INTRODUCTION

Nanocrystals (NCs) present broadly tunable optical features from visible to infrared range.[1] Compared to epitaxially grown materials, their colloidal synthesis releases the constraint of being epitaxially matched to a substrate. This eases the growth process as well as the coupling to read-out circuits for the design of focal plane arrays.[2−5] However, infrared sensors based on NCs keep suffering from a low carrier diffusion length, which makes charge collection inefficient for devices whose electrode separation is significantly larger than the diffusion length.[6] The resulting thin films are thus poorly photoresponsive, and light management strategies have to be introduced to absorb a significant part of the incident light into a NC slab whose size matches the diffusion length. In diodes based on vertical transport, absorption enhancement can be obtained by employing Fabry−Perot (F−P) cavities.[7,8] More advanced geometries have been proposed to harness the coupling with light,[9] including plasmonic cavities,[10−15] guided mode resonators,[16−19] F−P resonators,[20] metal−insulator−metal patches,[21−23] metasurfaces,[24,25] and combinations of these light resonators. By introducing the resonators, the absorption spectrum of the device can be reshaped with respect to that of the absorbing NCs. Absorption enhancement and spectral modification induced by a photonic structure are phenomena that are generally observed in semiconductor systems coupled to resonators or metasurfaces. Beyond these phenomena, another cavity-induced effect can be observed in NC-based devices, activated by the transport mechanisms peculiar to NC films. In a device consisting of a NC film coupled to a photonic structure, Dang et al.[21] observed a 15 meV blue shift of the photocurrent peak, fully reversible under bias application. The authors demonstrated that the photonic structure induces an inhomogeneous absorption within the NC film, and then the bias dependence of the charge collection tunes the spectral shape of the photoresponse. Even though the observed spectral shift was only 5% of the exciton peak line width, the possibility of using NCs as materials for active nanophotonics[26] is very interesting, in a field dominated by MEMS[27] and phase change materials.[28,29]

In this work, we investigate the different mechanisms governing the bias reconfigurability of a NC-based device, and we propose a detector showing a strong bias-dependent photoresponse. In order to design such a device, two different properties have been controlled: carrier transport and light

Received: May 16, 2022

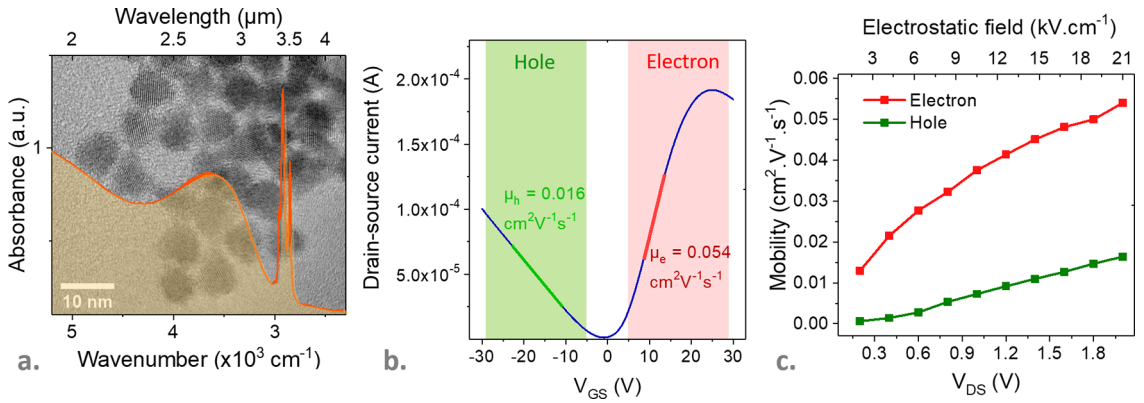

Figure 1. HgTe NCs and effect of electrostatic fields on carrier transport. (a). Room-temperature absorption spectrum of the HgTe NCs in solution. The background is a high-resolution transmission electron microscopy image of the HgTe NCs. (b). FET transfer curve as a function of gate potential when a bias of 2 V is applied between the drain and source electrodes, at 120 K. (c). Electron and hole mobilities as a function of drain−source bias at 120 K.

absorption. Concerning carrier transport, hopping conduction enables a transport diffusion length far below the device size. As a result, charge collection is more efficient in the vicinity of the electrodes. Here, we bring solid evidence of the bias dependence of the carrier mobility and thus of the diffusion length. The consequence of this observation is that the bias can be used as a knob to tune the device's active area. On the other hand, the absorbance of the device is spatially engineered through the use of a photonic structure. We show that, by coupling these two properties, we can use the diffusion length bias dependency to obtain a bias reconfigurable infrared sensor operating up to 240 K. Compared to previous work[21] (only a spectral shift was observed and only up to 120 K), we demonstrate a far more significant spectral reconfigurability now compatible with the relative amplitude modification of the optical resonances separated over an extended spectral window. Moreover, it is worth stressing that this result has been obtained in a device with a simple architecture by carefully engineering the size and periodicity of interdigitated electrodes on glass.

RESULTS AND DISCUSSION

Because the bias dependence of the carrier diffusion length is a central element in the design of a bias-reconfigurable photoresponse, we first study the effect of an electrostatic field on effective carrier mobilities in the NC arrays. On a Si/SiO_2 substrate, we build a field-effect transistor (FET) whose conductive channel comprises HgTe NC arrays.[30] A scheme of the FET device is indicated in Figure S2a with the NC film thickness of around 180 nm. The NCs are synthesized using the Prado et al. procedure.[31] The obtained particles present a spherical shape with a typical size of 8 nm, see Figures 1a and S1. The absorption spectrum of the NC solution shows a clear excitonic absorption around 3600 cm^{-1} (≈2.8 μm), along with a doublet around 2900 cm^{-1} due to the presence of capping ligands, see Figure 1a. Phase transfer is then performed[32,33] to exchange the initial long capping ligands for hybrid passivation combining short thiols and ions. Then, smooth, conductive NC films are prepared by spin-coating, see *Device Fabrication* in the Supporting Information. Figure 1b shows the FET transfer curve at 120 K. The NC film appears to be quasi-intrinsic with a minimum of conductance close to zero gate bias, and the transfer curve exhibits an ambipolar behavior with both hole (under negative gate bias) and electron (under positive gate bias) conduction regimes. At high gate voltages, a decrease of the drain−source current is observed, which is the characteristic of Pauli blocking at high electronic density.[33−35] As the temperature increases, the transfer curve shifts toward the negative side, indicating a n-doped film, see Figure S3. As our FET operates in the linear regime (Figure S2b), field-effect carrier mobilities are extracted using the linear region for a source−drain voltage V_{DS} negligible with respect to the gate voltage V_{GS}. In this regime, the mobility can be extracted as $\mu = \frac{L}{W \cdot C_i \cdot V_{DS}} \times \frac{\partial I_{DS}}{\partial V_{GS}}$, where L is the channel length, W is the channel width, C_i is the gate insulator capacitance per unit area (here, C_i = 11 nF cm^{-2} for a 300 nm SiO_2 layer), and I_{DS} is the drain−source current. Noticeably, we observe an increase in both electron and hole mobilities under an applied source−drain electric field. At 120 K, the electron mobility presents a 4-fold increase from 0.013 to 0.054 cm^2 V^{-1} s^{-1} when the drain−source bias is increased from 0.2 to 2 V. On the same range of bias voltages, the hole mobility shows an even more significant increase with a 26-fold increase from 6.2 × 10^{-4} to 0.016 cm^2 V^{-1} s^{-1}, see Figure 1c.

The bias dependence of mobility is observed from 120 to 240 K, see Figure S4. This increase of carrier mobility under applied electric field is rather significant. Nenashev et al., considering a hopping system with Miller−Abraham transition rates and Gaussian disorder model, show that $\mu(F)$, while solely depending on the charge carrier localization length, can be strongly enhanced under an applied electric field.[36] More recently, Xing et al. have suggested that the presence of positional disorders may enhance the carrier mobility by enabling the pathways across the NC film.[37] However, they anticipate that the carrier residence time on the NCs remains the same while only a slight increase of carrier mobilities with the electric field should be expected, contrary to our observations.

An increase of carrier mobility with increasing bias implies an increased carrier diffusion length (L_D), assuming that the carrier lifetime τ remains mostly unaffected by the application of an electric field. The Einstein relation links the diffusion coefficient D to the carrier mobility μ through $D = \mu k_B T/e$, with k_B being the Boltzmann constant, e the elementary charge, and T the temperature. This leads to $L_D=(D\cdot\tau)^{1/2}=(\mu k_B T/(e\cdot\tau))^{1/2}$, and thus, the 4- and 26-fold increase in mobility with bias in the range of our experiment corresponds to 2- and 5-

https://doi.org/10.1021/acsphotonics.2c00738
ACS Photonics XXXX, XXX, XXX−XXX

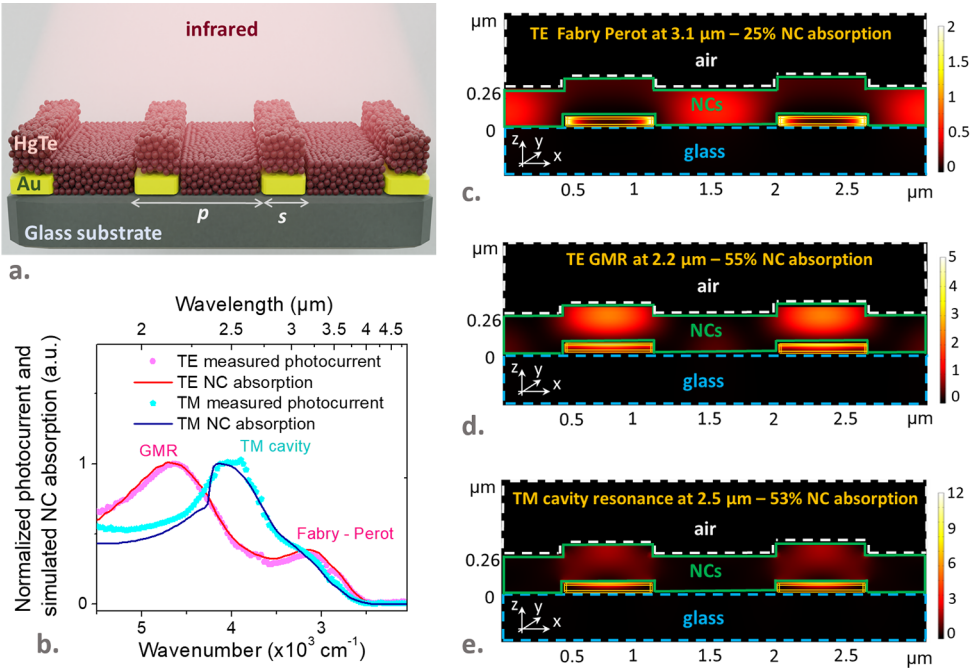

Figure 2. Design of the infrared sensor based on HgTe NCs. (a). Illustration of the HgTe NC infrared detector with grating geometry on a glass substrate. The optical properties of the device are defined by the grating period p and the stripe size s. (b). Comparison of the normalized photocurrent spectra and simulated NC absorption spectra under transverse electric and transverse magnetic polarizations. Here, TE and TM photocurrent spectra of the device are measured at 80 K and under 1.2 and 0.2 V bias voltages, respectively. See Figure S21c. (c). [resp. (d)] Absorption map associated with the F−P resonance (resp. GMR resonance) around 3.1 μm (resp. 2.5 μm) in TE polarization (TE—the electric field component in the y direction). (e). Absorption map associated with the resonance around 2.5 μm in TM polarization (TM—the magnetic field component in the y direction).

fold increase of the carrier diffusion lengths for electrons and holes, respectively.

In the following, we exploit the electric field dependence of the mobility to build a HgTe NC-based-photodetector allowing for a configurable photoresponse. Indeed, the bias applied to the photodetector modifies the value of the diffusion length, which in turn affects the spatial extent of the active region from which photoexcited carriers are collected. This gives rise to a device with reconfigurable response if the absorption of the NC film is inhomogeneous.[21] In order to implement a spatially inhomogeneous absorption, the NC array is coupled to a grating resonator which has a dual role of collecting photoexcited carriers and generating multiple absorption resonances.

The geometry of our detector is depicted in Figure 2a. Despite being a simple geometry, the grating coupled to the NC film offers several degrees of freedom for the design of the light-matter coupling (i.e., the grating period p, the electrode size s, and the film thickness t_{NC}). On a glass substrate, we fabricate the gold grating using electron beam lithography before functionalizing the structure with a film of HgTe NCs for photodetection in the short- and mid-wave infrared. The design is guided by finite element method simulations, see *Finite element method simulation and design of the device* in the Supporting Information.

Our objective is to design at least two electromagnetic modes: one located in the vicinity of the electrodes in order for generated photocarriers to be collected under low applied electric fields, while the other one is located away from the electrodes to generate photocarriers that will only be collected under higher electric fields. The latter mode is designed by taking advantage of the impedance mismatch between the NC film in the openings between the electrodes and the ones on top of the gold. Under TE polarization, a FP resonance, spatially located between the electrodes, can be generated as long as the gold and NC film thicknesses are well chosen, see Figures 2c and S6−S7. The resonance wavelength of this mode is driven by the opening size $o = p - s = 2 \cdot n_{eff} \cdot \lambda_{FP}$, where n_{eff} is the effective index of the mode. Here, this resonance is also matched with the NC exciton, with a peak around 3.1 μm, as shown in the absorption spectrum in Figure 2b. We then design the mode located nearby the electrodes. Thanks to the presence of the grating, the incoming light can be coupled with a waveguide mode.[16−18,38] By carefully choosing the grating period p, diffraction orders in the NC layer can couple to a guided mode, referred to as a guided-mode resonance (GMR). More importantly, the GMR focuses light on the NCs above the grating stripes and features a resonant peak around 2.2 μm, see Figure 2d. The nature of the GMR is revealed by its dispersive characteristic, see the dispersion maps in Figure S8. Detailed analysis and calculations on the GMR can be found in Figures S5−S8. With the two modes designed to be separated spectrally and spatially, we hence expect to see bias reconfigurability when the device is illuminated under TE polarization. Let us now discuss the resonance around 2.5 μm in TM polarization in Figure 2b. This resonance, referred to as TM cavity resonance, strongly enhances the electromagnetic field and absorption of the NC film above the electrodes, see Figures 2e and S10a. One can also notice a feature at around 3 μm that corresponds to the NC band edge after ligand exchange. Expectedly, the simulated NC absorption in the slits is negligible, see our simulated spectra in Figure S10b. Therefore, a negligible voltage dependence is anticipated for the device photoresponse under TM polarization. A compar-

https://doi.org/10.1021/acsphotonics.2c00738
ACS Photonics XXXX, XXX, XXX−XXX

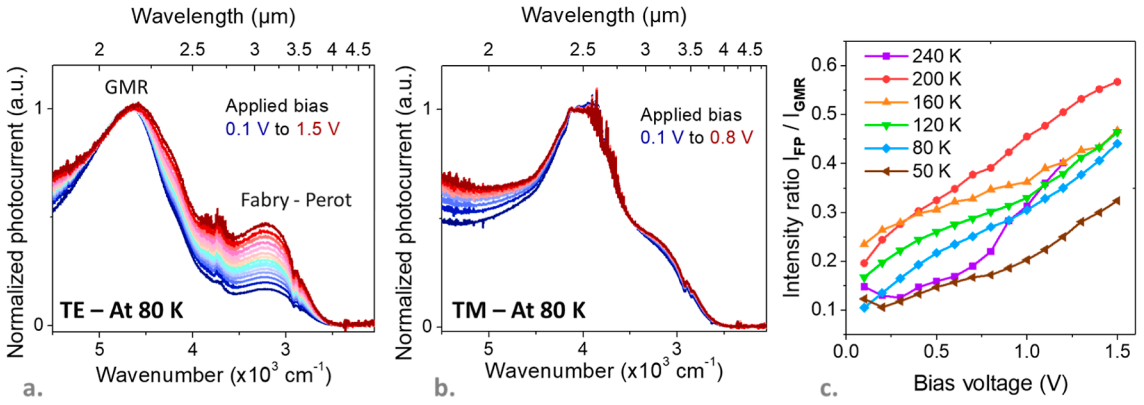

Figure 3. Bias tunability of the device. (a) Photocurrent spectra of the device in TE polarization under various applied biases from 0.1 to 1.5 V (step of 0.1 V) at 80 K. (b). Photocurrent spectra of the device in TE polarization under various applied biases from 0.1 to 0.8 V (step of 0.1 V) at 80 K. (c). Intensity ratio between the F–P resonance and the GMR in TE polarization as a function of applied bias at various temperatures.

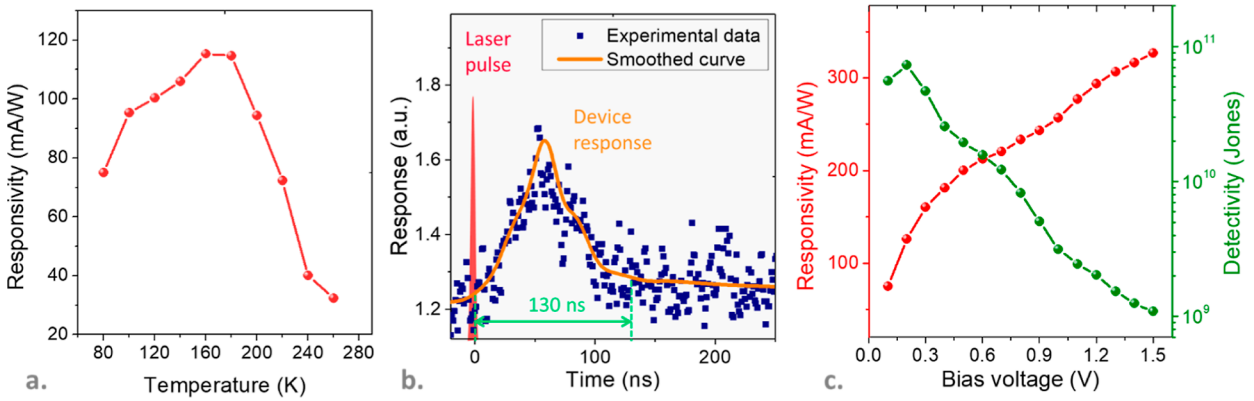

Figure 4. Photodetection performance. (a) Responsivity of the device under broadband illumination (blackbody at 980 °C) as a function of the temperature when biased with 0.1 V. (b). Photoresponse of the device when illuminated with 1.2 ns laser pulses (λ = 1.57 μm) at 80 K. (c). Responsivity of the device under broadband illumination (blackbody at 980 °C) and detectivity (at 1 kHz) of the device as a function of the applied bias at 80 K.

ison of electric field distributions for the TE and TM resonances is presented in Figure S12 along with color maps shown in Figures S6 and S10.

The set of geometrical parameters used for the fabrication of the grating corresponds to a grating period p and stripe size s of 1.6 and 0.95 μm, respectively, see Figures S14 and 15 for microscopy images, while the HgTe film has a thickness of 270 nm. Figure 2b compares simulated NC absorption spectra with the measured device's photoresponse. Under both TE and TM polarizations, the experimental and simulated spectra show an excellent agreement in the targeted range from 1.5 to 4.0 μm.

Figure 3a,b shows the normalized photocurrent spectra of the device as a function of various bias voltages at 80 K. As expected, an apparent tunable photoresponse with applied bias can be observed under TE polarization. In contrast, no significant change of the photocurrent spectrum is observed when the incident light is TM polarized. As the applied bias increases, the ratio between the intensity of the TE F–P resonance and the intensity of the GMR grows from 0.1 for a bias of 0.1 V to 0.44 for a bias of 1.5 V. Note that this spectral modulation is fully reversible (i.e., the peak intensity ratio decreases when the applied bias decreases) and is not dependent on the bias polarity. Here, the Stark effect can be excluded as a possible mechanism to explain the origin of this bias reconfigurability since it requires an electric field above 100 kV cm^{-1} to generate a much smaller band edge shift,[6,21] also see Figure S20. Moreover, the Stark effect will affect both polarizations the same way.

The bias dependence of the spectral response of our device under TE polarization is observed in a wide range of temperatures from 50 to 240 K, see Figures 3c and S17, while the shape of TM photocurrent spectrum remains almost unchanged, see Figure S19. Compared to previous work,[21] it should be pointed out that the spectral change is far more dramatic. Furthermore, we are able to induce relative photocurrent magnitude reconfiguration, while before, only a small spectral shift was observed. In addition, the careful engineering of the absorption allows observing the effect over a much broader range of temperatures (up to 240 K) compared to 120 K in the previous device.

To this point, it should be noted that the intensity ratio of the two TE resonances increases when the photocurrent signal from both resonances also increases with the applied bias, see Figures S16 and S18. We attribute this modulation to different degrees of overlap between electromagnetic resonances and the induced electrostatic field. Since the grating is used as interdigitated electrodes, the in-plane electric field component dominates, and a greater field strength is established in the slits between the neighboring electrodes, see Figure S11. Under low electric fields, charge collection mainly occurs near the electrodes, which favors the spectral weight of the nearby resonance, evidenced by a stronger spectral weight of the GMR

https://doi.org/10.1021/acsphotonics.2c00738
ACS Photonics XXXX, XXX, XXX–XXX

Table 1. Figures of Merit for HgTe NC Sensors with Designed Light-Matter Coupling

material	device design	spectral range/cut-off wavelength	responsivity (mA/W)	time response	D[a] (Jones)	operating temperature (K)	references
HgTe CdSe	gate-switchable photoresponse	visible/SWIR 2.5 μm	0.17			300	39
HgTe	coupling to plasmon	MWIR 4−5 μm	190		1.52×10^{10}	80	11
HgTe	plasmon+ F−P	MWIR 4.5−5 μm	1620		4×10^{11}	85	10
HgTe	F−P	SWIR 2.2 μm	500	260 ns	7.5×10^{10}	300	7
HgTe	dual band stacked photodiode	SWIR/MWIR 4−5 μm	400	2.5 μs[a]	3×10^{11}	85	40
HgTe	coupling to cavity to achieve 64 narrow bands	SWIR 2.08 μm	200	120 ns	10^{10}	295	20
HgTe	coupling to plasmon	SWIR 2.3 μm	23		3.2×10^{6}	300	13
HgTe PbS	guided mode resonator	SWIR and extended SWIR 3 μm	1000		10^{10}	200	18
HgTe	bias shiftable photoresponse	MWIR 3.5−4 μm	60	5 μs[a]	8×10^{9}	80	21
HgTe	three resonances induced by GMR	SWIR 3 μm		14 μs[a]	10^{12}	30	16
HgSe/HgTe	intraband photodiode	MWIR/SWIR 5 μm	5	500 ns	1.5×10^{9}	80	41
HgSe/HgTe	spray—stencil fabricated photodiode	MWIR/SWIR 5 μm	400	6.4 μs	2×10^{10}	80	42
HgTe	bias-modulated spectral response with basic grating geometry	MWIR 4 μm	320	70 ns	7×10^{10}	80	this work

[a]Reported values is setup-limited.

in Figure 3a. When a large electric field is applied, charge collection becomes more efficient, and the spectral weight associated with the TE F−P resonance, spatially localized away from the electrodes, increases.

The drastic change in intensity ratio also raises a crucial point in the design of a NC-based infrared sensor, which so far has been mainly focused on enhancing material absorption using optical resonators. In fact, it shows that spatially designing the resonance to be well aligned with the applied electrostatic field is also essential for efficient charge extraction, indicating that the optical modes can be effectively exploited. However, it is noteworthy that although the TE F−P resonance field (Figure 2c) fits better with the electrostatic field map (Figure S11a) than for TE GMR resonance (Figure 2d), the photocurrent is higher at GMR resonance because the field enhancement is higher.

The photodetection performance of the device is then characterized. The responsivity under broadband radiation (blackbody at 980 °C) appears to depend strongly on the temperature. The measured responsivity of the device reaches a maximum of ≈110 mA W^{-1} at around 160−180 K when a bias of 0.1 V is applied, see Figure 4a. Noticeably, we observe a significant decrease of responsivity when the temperature goes higher than 200 K for a series of devices fabricated using the same material. This decrease can be attributed to the drop in electron mobility above 200 K, as shown in Figure S4. Fitting the dark current−temperature dependence to the Arrhenius equation gives an estimated activation energy of around 150 meV, close to half of the material band-edge energy (≈180 meV), see Figure S21a. The dark current thus drastically reduces upon cooling. The $I-V$ curve under dark condition is linear at 280 K and appears more superlinear at low temperatures, see Figure S21b. A typical transient response of the device to 1.2 ns laser pulse using a 1.57 μm laser source is shown in Figure 4b, where a quick increase in the photocurrent is followed by a slower drop to the dark current values. The rise time is around 60 ns, while the decay process is estimated to be around 70 ns. For photoconductive devices, the signal-to-noise ratio of the detectors improves at low temperatures thanks to the reduction of dark current. At 80 K, the $1/f$ noise prevails in the noise spectrum of our device, see Figure S22. Figure 4c presents the responsivity and detectivity (at 1 kHz) of the device operating at 80 K as functions of the applied bias. The responsivity increases monotonically from 70 to 320 mA W^{-1} when the bias increases from 0.1 to 1.5 V. On the other hand, the detectivity peaks at 7×10^{10} Jones for 0.2 V applied bias before steadily lowering while maintaining a value of more than 10^{9} Jones up to 1.5 V. Table 1 compares the performances of the recently developed HgTe NC-based photodetectors, including our device. Our device, which can be straightforward for fabrication process thanks to the basic geometry design, presents a shorter response time compared to the reported mid-wave infrared detectors while retaining a highly competitive detectivity at low-temperature operation.

CONCLUSIONS

To summarize, we bring evidence for bias dependence of carrier mobilities in the HgTe NCs film. This property and an inhomogeneous absorption in NC-based devices are critical ingredients for bias-reconfigurable photoresponse in photodetectors. We then fabricated a device using a simple grating geometry, which exhibits a strong tunable photoresponse as a function of bias over a wide range of temperatures from 50 to 240 K. The significant response tunability can be achieved in our device thanks to the dynamic control of the device's active area with the applied bias. The obtained infrared sensing device also presents a detectivity of 7×10^{10} Jones at 80 K and 1 kHz with 4 μm cutoff wavelength and around 70 ns response time. Our work lays the groundwork for further studies in the field of active photonic systems based on NCs.

METHODS

Chemicals. Mercury chloride ($HgCl_2$, Sigma-Aldrich, 99%), mercury bromide ($HgBr_2$, Alfa Aesar), tellurium powder (Te, Sigma-Aldrich, 99.99%), trioctylphosphine (TOP, Alfa, 90%), oleylamine (OLA, Acros, 80−90%), dodecanethiol (DDT, Sigma-Aldrich, 98%), 2-mercaptoethanol (MPOH, Merck, >99%), N,N-dimethylformamide (DMF, VWR), and toluene (VWR, 99.8%) were used. All chemicals were used without further purification, except oleylamine that is centrifuged before use. Mercury compounds are highly toxic. Handle them with special care.

1 M TOP/Te Precursor. Te powder (2.54 g) was mixed in 20 mL of TOP in a three-neck flask. The flask was kept under

https://doi.org/10.1021/acsphotonics.2c00738
ACS Photonics XXXX, XXX, XXX−XXX

vacuum at room temperature for 5 min, and then the temperature was raised to 100 °C. Next, degassing of the flask was conducted for the next 20 min. The atmosphere was switched to nitrogen, and the temperature was raised to 275 °C. The solution was stirred until a clear orange color was obtained. The flask was cooled to room temperature, and the color changed to yellow. Finally, this solution was transferred to a nitrogen-filled glove box for storage.

HgTe NC Growth. In a 50 mL three-neck flask, 18 mL of oleylamine was degassed under vacuum and heated to 120 °C for 1 h. Then, the atmosphere was switched to N_2, and the temperature was set at 120 °C. Meanwhile, in a vial, 72 mg of $HgBr_2$ (0.2 mmol) was dissolved in 1.8 mL of OLA under sonication. After degassing, the solution, 0.2 mL of TOP/Te (1 M), was added ($t_w = 0$). Next, after a waiting time of $t_w = 10$ min, the solution was transferred to the syringe, and the content was quickly introduced into hot OLA (120 °C). The solution color quickly turned dark brown. After 3 min, a cold mixture (i.e., freezer cooled) of 1 mL DDT in 2 mL of toluene was injected, and an ice bath was used to decrease the temperature quickly. The content of the flask was transferred to a centrifuge tube, and QDs were precipitated by adding methanol. After centrifugation, the formed pellet was redispersed in toluene. The solution was precipitated a second time with absolute ethanol and redispersed in toluene. At this step, the QDs were centrifuged in toluene to eliminate the lamellar phase. The solid phase was discarded, and the stable solution phase was transferred to a weighed centrifuge tube and finally precipitated using methanol. Again, the formed pellet (45 mg of dried powder was typically obtained) was redispersed in toluene.

HgTe Ink Preparation. $HgCl_2$ (20 mg), 2 mL of MPOH, and 18 mL of DMF were mixed to form an exchange solution. This exchange solution (0.25 mL) and 0.5 mL of DMF were added to 0.25 mL of HgTe NCs in toluene. Phase dissociation occurred when a few drops of hexane were added to the mixture: the dark bottom phase is where the NCs migrate, while the top transparent phase can be removed with a plastic pipette. This washing step was repeated twice before the addition of a few milliliters of toluene, and the mixture was centrifuged at 6000 rpm for 4 min. The supernatant was discarded, while the formed solid pellets of NCs were redispersed in 100 μL of DMF to obtain the ink of HgTe. A few cycles of sonication−vortex−centrifugation can help to promote particle dispersion.

Spectral Photoresponse. Spectral photoresponse was measured with a Fisher IS50 FTIR while the sample was biased with a Femto DLPCA 200 amplifier, which was also used for amplifying the photocurrent signal before sending the signal back into the FTIR for spectral analysis. The spectra were typically obtained in the continuous scan mode with 4 cm^{-1} resolution and averaged at least 32 times.

Responsivity. Responsivity was measured with a blackbody at 980 °C as the infrared source. The sample was placed around 24 cm from the blackbody, and the incoming flux was modulated by an optical chopper with frequency set to 1000 Hz. A Ge window filtering out all wavelengths shorter than 1.9 μm was placed between the source and the sample. The incident power was then calculated as

$$P(W) = \pi A_{det} \cdot \sin^2\theta/2 \cdot \cos\varphi \cdot \int_{1.9\mu m}^{\lambda_{cut\text{-}off}} \frac{2hc^2}{\lambda^5} \frac{1}{\exp\left(\frac{hc}{\lambda kT}\right) - 1} d\lambda$$

where A_{det} is the area of the photodetector, θ is the field of view, φ is the incident angle (typically assumed to be 0°), h is the Planck constant, c is the speed of light, k is the Boltzmann constant, and T is the blackbody temperature equal to 980 °C. $\lambda_{cut\text{-}off}$ is taken from the absorption edge of the material.

Response Time Measurement. The photocurrent signal from the sample (inside the cryostat, placed under voltage bias) was amplified with a DUPVA-1-70 amplifier and then fed to an oscilloscope. The pulses were generated by a 1573 nm Q-switched pulse laser diode from a CNI laser with 100 Hz repetition rate and 1.2 ns pulse duration.

Noise Measurement. Noise measurement was conducted with an SR780 spectrum analyzer while the device was biased with a Femto DLPCA 200 amplifier. The noise spectra were typically acquired over a frequency from 10 Hz to 1.6 kHz. Typically, the noise current density spectrum was obtained after averaging 100 scans.

Detectivity. Detectivity is computed from $D^* = \frac{\mathcal{R}\sqrt{A}}{S_I}$, where $\mathcal{R}$ is the responsivity of the device, A is the device area (i.e., 3.5×10^{-4} cm^2), and S_I is the measured noise current density.

■ ASSOCIATED CONTENT

Supporting Information

The Supporting Information is available free of charge at https://pubs.acs.org/doi/10.1021/acsphotonics.2c00738.

Material characterization, electromagnetic simulation and device design, and device fabrication procedure (PDF)

■ AUTHOR INFORMATION

Corresponding Authors

Angela Vasanelli − *Laboratoire de Physique de l'Ecole Normale Supérieure, ENS, Université PSL, CNRS, Sorbonne Université, Université Paris Cité, Paris 75005, France*; Email: angela.vasanelli@ens.fr

Emmanuel Lhuillier − *Sorbonne Université, CNRS, Institut des NanoSciences de Paris, INSP, Paris 75005, France*; orcid.org/0000-0003-2582-1422; Email: el@insp.upmc.fr

Authors

Tung Huu Dang − *Laboratoire de Physique de l'Ecole Normale Supérieure, ENS, Université PSL, CNRS, Sorbonne Université, Université Paris Cité, Paris 75005, France; Sorbonne Université, CNRS, Institut des NanoSciences de Paris, INSP, Paris 75005, France*; orcid.org/0000-0003-0310-9004

Adrien Khalili − *Sorbonne Université, CNRS, Institut des NanoSciences de Paris, INSP, Paris 75005, France*; orcid.org/0000-0001-5685-9963

Claire Abadie − *Sorbonne Université, CNRS, Institut des NanoSciences de Paris, INSP, Paris 75005, France*; orcid.org/0000-0003-4309-9488

https://doi.org/10.1021/acsphotonics.2c00738
ACS Photonics XXXX, XXX, XXX−XXX

Charlie Gréboval − *Sorbonne Université, CNRS, Institut des NanoSciences de Paris, INSP, Paris 75005, France;* orcid.org/0000-0002-0314-7273
Mariarosa Cavallo − *Sorbonne Université, CNRS, Institut des NanoSciences de Paris, INSP, Paris 75005, France;* orcid.org/0000-0002-8768-5545
Huichen Zhang − *Sorbonne Université, CNRS, Institut des NanoSciences de Paris, INSP, Paris 75005, France;* orcid.org/0000-0001-5346-0148
Erwan Bossavit − *Sorbonne Université, CNRS, Institut des NanoSciences de Paris, INSP, Paris 75005, France;* orcid.org/0000-0001-6088-3309
James K. Utterback − *Sorbonne Université, CNRS, Institut des NanoSciences de Paris, INSP, Paris 75005, France;* orcid.org/0000-0002-2926-841X
Erwan Dandeu − *Sorbonne Université, CNRS, Institut des NanoSciences de Paris, INSP, Paris 75005, France*
Yoann Prado − *Sorbonne Université, CNRS, Institut des NanoSciences de Paris, INSP, Paris 75005, France;* orcid.org/0000-0001-6228-2486
Gregory Vincent − *ONERA—The French Aerospace Lab, Palaiseau 91123, France;* orcid.org/0000-0003-1636-3853
Sandrine Ithurria − *Laboratoire de Physique et d'Etude des Matériaux, ESPCI-Paris, PSL Research University, Sorbonne Université UPMC Univ Paris 06, CNRS, Paris 75005, France;* orcid.org/0000-0002-4733-9883
Yanko Todorov − *Laboratoire de Physique de l'Ecole Normale Supérieure, ENS, Université PSL, CNRS, Sorbonne Université, Université Paris Cité, Paris 75005, France*
Carlo Sirtori − *Laboratoire de Physique de l'Ecole Normale Supérieure, ENS, Université PSL, CNRS, Sorbonne Université, Université Paris Cité, Paris 75005, France*

Complete contact information is available at: https://pubs.acs.org/10.1021/acsphotonics.2c00738

Funding

The project was supported by ERC starting grants blackQD (grant no: 756225). We acknowledge the use of clean-room facilities at the "Centrale de Proximité Paris-Centre". This work has been supported by Region Ile-de-France in the framework of DIM Nano-K (grant dopQD). This work was supported by French state funds managed by the ANR within the Investissements d'Avenir programme under reference ANR-11-IDEX-0004-02 and, more specifically, within the framework of the Cluster of Excellence MATISSE and by grants IPER-Nano2 (ANR-18CE30-0023-01), Copin (ANR-19-CE24-0022), Frontal (ANR-19-CE09-0017), Graskop (ANR-19-CE09-0026), NITQuantum (ANR-20-ASTR-0008-01), Bright (ANR-21-CE24-0012-02), and MixDferro (ANR-21-CE09-0029).

Notes

The authors declare no competing financial interest.

REFERENCES

(1) Lu, H.; Carroll, G. M.; Neale, N. R.; Beard, M. C. Infrared Quantum Dots: Progress, Challenges, and Opportunities. *ACS Nano* **2019**, *13*, 939−953.
(2) Rauch, T.; Böberl, M.; Tedde, S. F.; Fürst, J.; Kovalenko, M. V.; Hesser, G.; Lemmer, U.; Heiss, W.; Hayden, O. Near-Infrared Imaging with Quantum-Dot-Sensitized Organic Photodiodes. *Nat. Photonics* **2009**, *3*, 332−336.
(3) Chu, A.; Martinez, B.; Ferré, S.; Noguier, V.; Gréboval, C.; Livache, C.; Qu, J.; Prado, Y.; Casaretto, N.; Goubet, N.; Cruguel, H.; Dudy, L.; Silly, M. G.; Vincent, G.; Lhuillier, E. HgTe Nanocrystals for SWIR Detection and Their Integration up to the Focal Plane Array. *ACS Appl. Mater. Interfaces* **2019**, *11*, 33116−33123.
(4) Ciani, A. J.; Pimpinella, R. E.; Grein, C. H.; Guyot-Sionnest, P. Colloidal Quantum Dots for Low-Cost MWIR Imaging. *Infrared Phys. Technol.* **2016**, *9819*, 981919.
(5) Pejovi, V.; Georgitzikis, E.; Lee, J.; Lieberman, I.; Cheyns, D.; Heremans, P.; Malinowski, P. E. Infrared Colloidal Quantum Dot Image Sensors. *IEEE Trans. Electron Devices* **2021**, *69*, 2840−2850.
(6) Chu, A.; Gréboval, C.; Prado, Y.; Majjad, H.; Delerue, C.; Dayen, J.-F.; Vincent, G.; Lhuillier, E. Infrared Photoconduction at the Diffusion Length Limit in HgTe Nanocrystal Arrays. *Nat. Commun.* **2021**, *12*, 1794.
(7) Tang, X.; Ackerman, M. M.; Shen, G.; Guyot-Sionnest, P. Towards Infrared Electronic Eyes: Flexible Colloidal Quantum Dot Photovoltaic Detectors Enhanced by Resonant Cavity. *Small* **2019**, *15*, 1804920.
(8) Ramade, J.; Qu, J.; Chu, A.; Gréboval, C.; Livache, C.; Goubet, N.; Martinez, B.; Vincent, G.; Lhuillier, E. Potential of Colloidal Quantum Dot Based Solar Cells for Near-Infrared Active Detection. *ACS Photonics* **2020**, *7*, 272−278.
(9) Chen, M.; Lu, L.; Yu, H.; Li, C.; Zhao, N. Integration of Colloidal Quantum Dots with Photonic Structures for Optoelectronic and Optical Devices. *Adv. Sci.* **2021**, *8*, 2101560.
(10) Tang, X.; Ackerman, M. M.; Guyot-Sionnest, P. Thermal Imaging with Plasmon Resonance Enhanced HgTe Colloidal Quantum Dot Photovoltaic Devices. *ACS Nano* **2018**, *12*, 7362−7370.
(11) Yifat, Y.; Ackerman, M.; Guyot-Sionnest, P. Mid-IR Colloidal Quantum Dot Detectors Enhanced by Optical Nano-Antennas. *Appl. Phys. Lett.* **2017**, *110*, 041106.
(12) Tang, X.; Wu, G. f.; Lai, K. W. C. Plasmon Resonance Enhanced Colloidal HgSe Quantum Dot Filterless Narrowband Photodetectors for Mid-Wave Infrared. *J. Mater. Chem. C* **2017**, *5*, 362−369.
(13) Zhu, B.; Chen, M.; Zhu, Q.; Zhou, G.; Abdelazim, N. M.; Zhou, W.; Kershaw, S. V.; Rogach, A. L.; Zhao, N.; Tsang, H. K. Integrated Plasmonic Infrared Photodetector Based on Colloidal HgTe Quantum Dots. *Adv. Mater. Technol.* **2019**, *4*, 1900354.
(14) Wang, H.; Guo, Y.; Hao, H.; Bian, H.; Aubin, H.; Wei, Y.; Li, H.; Liu, T.; Degiron, A.; Wang, H. Bright CdSe/CdS Quantum Dot Light-Emitting Diodes with Modulated Carrier Dynamics via the Local Kirchhoff Law. *ACS Appl. Mater. Interfaces* **2021**, *13*, 56476−56484.
(15) Wang, H.; Guo, Y.; Zang, J.; Hao, H.; Wang, L.; Liu, T.; Bian, H.; Jiang, R.; Wen, R.; Li, H.; Tong, Y.; Wang, H. Nanoantennas Involved Optical Plasmonic Cavity for Improved Luminescence of Quantum Dots Light-Emitting Diodes. *ACS Appl. Mater. Interfaces* **2021**, *13*, 44760−44767.
(16) Gréboval, C.; Chu, A.; Magalhaes, D. V.; Ramade, J.; Qu, J.; Rastogi, P.; Khalili, A.; Chee, S. S.; Aubin, H.; Vincent, G.; Bals, S.; Delerue, C.; Lhuillier, E. Ferroelectric Gating of Narrow Band-Gap Nanocrystal Arrays with Enhanced Light-Matter Coupling. *ACS Photonics* **2021**, *8*, 259−268.
(17) Rastogi, P.; Chu, A.; Gréboval, C.; Qu, J.; Noumbé, U. N.; Chee, S.-S.; Goyal, M.; Khalili, A.; Xu, X. Z.; Cruguel, H.; Ithurria, S.; Gallas, B.; Dayen, J.-F.; Dudy, L.; Silly, M. G.; Patriarche, G.; Degiron, A.; Vincent, G.; Lhuillier, E. Pushing Absorption of Perovskite Nanocrystals into the Infrared. *Nano Lett.* **2020**, *20*, 3999−4006.
(18) Chu, A.; Gréboval, C.; Goubet, N.; Martinez, B.; Livache, C.; Qu, J.; Rastogi, P.; Bresciani, F. A.; Prado, Y.; Suffit, S.; Ithurria, S.; Vincent, G.; Lhuillier, E. Near Unity Absorption in Nanocrystal Based Short Wave Infrared Photodetectors Using Guided Mode Resonators. *ACS Photonics* **2019**, *6*, 2553−2561.
(19) Rastogi, P.; Chu, A.; Dang, T. H.; Prado, Y.; Gréboval, C.; Qu, J.; Dabard, C.; Khalili, A.; Dandeu, E.; Fix, B.; Xu, X. Z.; Ithurria, S.; Vincent, G.; Gallas, B.; Lhuillier, E. Complex Optical Index of HgTe

Nanocrystal Infrared Thin Films and Its Use for Short Wave Infrared Photodiode Design. *Adv. Opt. Mater.* **2021**, *9*, 2002066.
(20) Tang, X.; Ackerman, M. M.; Guyot-Sionnest, P. Acquisition of Hyperspectral Data with Colloidal Quantum Dots. *Laser Photonics Rev.* **2019**, *13*, 1900165.
(21) Dang, T. H.; Vasanelli, A.; Todorov, Y.; Sirtori, C.; Prado, Y.; Chu, A.; Gréboval, C.; Khalili, A.; Cruguel, H.; Delerue, C.; Vincent, G.; Lhuillier, E. Bias Tunable Spectral Response of Nanocrystal Array in a Plasmonic Cavity. *Nano Lett.* **2021**, *21*, 6671−6677.
(22) Caligiuri, V.; Palei, M.; Imran, M.; Manna, L.; Krahne, R. Planar Double-Epsilon-Near-Zero Cavities for Spontaneous Emission and Purcell Effect Enhancement. *ACS Photonics* **2018**, *5*, 2287−2294.
(23) Caligiuri, V.; Biffi, G.; Palei, M.; Martín-García, B.; Pothuraju, R. D.; Bretonnière, Y.; Krahne, R. Angle and Polarization Selective Spontaneous Emission in Dye-Doped Metal/Insulator/Metal Nanocavities. *Adv. Opt. Mater.* **2020**, *8*, 1901215.
(24) Đorđević, N.; Schwanninger, R.; Yarema, M.; Koepfli, S.; Yarema, O.; Salamin, Y.; Lassaline, N.; Cheng, B.; Yazdani, N.; Dorodnyy, A.; Fedoryshyn, Y. M.; Wood, V.; Leuthold, J. Metasurface Colloidal Quantum Dot Photodetectors. *ACS Photonics* **2022**, *9*, 482−492.
(25) Caillas, A.; Suffit, S.; Filloux, P.; Lhuillier, E.; Degiron, A. Anomalous Absorption in Arrays of Metallic Nanoparticles: A Powerful Tool for Quantum Dot Optoelectronics. *Nano Lett.* **2022**, *22*, 8−13.
(26) Krasnok, A.; Alu, A. Active Nanophotonics. *Proc. IEEE* **2020**, *108*, 628−654.
(27) Stark, T.; Imboden, M.; Kaya, S.; Mertiri, A.; Chang, J.; Erramilli, S.; Bishop, D. MEMS Tunable Mid-Infrared Plasmonic Spectrometer. *ACS Photonics* **2016**, *3*, 14−19.
(28) Shi, X.; Chen, C.; Liu, S.; Li, G. Nonvolatile, Reconfigurable and Narrowband Mid-Infrared Filter Based on Surface Lattice Resonance in Phase-Change Ge2sb2te5. *Nanomaterials* **2020**, *10*, 2530.
(29) Pogrebnyakov, A. V.; Bossard, J. A.; Turpin, J. P.; Musgraves, J. D.; Shin, H. J.; Rivero-Baleine, C.; Podraza, N.; Richardson, K. A.; Werner, D. H.; Mayer, T. S. Reconfigurable Near-IR Metasurface Based on Ge 2 Sb 2 Te 5 Phase-Change Material. *Opt. Mater. Express* **2018**, *8*, 2264.
(30) Gréboval, C.; Chu, A.; Goubet, N.; Livache, C.; Ithurria, S.; Lhuillier, E. Mercury Chalcogenide Quantum Dots : Material Perspective for Device Integration. *Chem. Rev.* **2021**, *121*, 3627−3700.
(31) Prado, Y.; Qu, J.; Gréboval, C.; Dabard, C.; Rastogi, P.; Chu, A.; Khalili, A.; Xu, X. Z.; Delerue, C.; Ithurria, S.; Lhuillier, E. Seeded Growth of HgTe Nanocrystals for Shape Control and Their Use in Narrow Infrared Electroluminescence. *Chem. Mater.* **2021**, *33*, 2054−2061.
(32) Martinez, B.; Ramade, J.; Livache, C.; Goubet, N.; Chu, A.; Gréboval, C.; Qu, J.; Watkins, W. L.; Becerra, L.; Dandeu, E.; Fave, J. L.; Méthivier, C.; Lacaze, E.; Lhuillier, E. HgTe Nanocrystal Inks for Extended Short-Wave Infrared Detection. *Adv. Opt. Mater.* **2019**, *7*, 1900348.
(33) Lan, X.; Chen, M.; Hudson, M. H.; Kamysbayev, V.; Wang, Y.; Guyot-Sionnest, P.; Talapin, D. V. Quantum Dot Solids Showing State-Resolved Band-like Transport. *Nat. Mater.* **2020**, *19*, 323−329.
(34) Hudson, M. H.; Chen, M.; Kamysbayev, V.; Janke, E. M.; Lan, X.; Allan, G.; Delerue, C.; Lee, B.; Guyot-Sionnest, P.; Talapin, D. V. Conduction Band Fine Structure in Colloidal HgTe Quantum Dots. *ACS Nano* **2018**, *12*, 9397−9404.
(35) Yu, D.; Wang, C.; Guyot-Sionnest, P. N-Type Conducting CdSe Nanocrystal Solids. *Science* **2003**, *300*, 1277−1280.
(36) Nenashev, A. V.; Oelerich, J. O.; Dvurechenskii, A. V.; Gebhard, F.; Baranovskii, S. D. Fundamental Characteristic Length Scale for the Field Dependence of Hopping Charge Transport in Disordered Organic Semiconductors. *Phys. Rev. B* **2017**, *96*, 035204.
(37) Xing, Y.; Yazdani, N.; Lin, W. M. M.; Yarema, M.; Zahn, R.; Wood, V. Effect of Positional Disorders on Charge Transport in Nanocrystal Quantum Dot Thin Films. *ACS Appl. Mater. Interfaces* **2022**, *4*, 631−642.
(38) Wang, S. S.; Magnusson, R. Theory and Applications of Guided-Mode Resonance Filters. *Appl. Opt.* **1993**, *32*, 2606.
(39) Lhuillier, E.; Robin, A.; Ithurria, S.; Aubin, H.; Dubertret, B. Electrolyte-Gated Colloidal Nanoplatelets-Based Phototransistor and Its Use for Bicolor Detection. *Nano Lett.* **2014**, *14*, 2715−2719.
(40) Tang, X.; Ackerman, M. M.; Chen, M.; Guyot-Sionnest, P. Dual-Band Infrared Imaging Using Stacked Colloidal Quantum Dot Photodiodes. *Nat. Photonics* **2019**, *13*, 277−282.
(41) Livache, C.; Martinez, B.; Goubet, N.; Gréboval, C.; Qu, J.; Chu, A.; Royer, S.; Ithurria, S.; Silly, M. G.; Dubertret, B.; Lhuillier, E. A Colloidal Quantum Dot Infrared Photodetector and Its Use for Intraband Detection. *Nat. Commun.* **2019**, *10*, 2125.
(42) Zhang, S.; Chen, M.; Mu, G.; Li, J.; Hao, Q.; Tang, X. Spray-Stencil Lithography Enabled Large-Scale Fabrication of Multispectral Colloidal Quantum-Dot Infrared Detectors. *Adv. Mater. Technol.* **2022**, *7*, 2101132.

https://doi.org/10.1021/acsphotonics.2c00738
ACS Photonics XXXX, XXX, XXX−XXX